Toward establishing low-lying Λ and Σ hyperon resonances with the K[over ¯]+d→π+Y+N reaction

H. Kamano and T.-S. H. Lee

Towards establishing low-lying Λ and Σ hyperon resonances with $\bar{K} + d \to \pi + Y + N$ reaction

H. Kamano[1,2] and T.-S. H. Lee[3]

[1]*KEK Theory Center, Institute of Particle and Nuclear Studies (IPNS),*
High Energy Accelerator Research Organization (KEK), Tsukuba, Ibaraki 305-0801, Japan
[2]*J-PARC Branch, KEK Theory Center,*
IPNS, KEK, Tokai, Ibaraki 319-1106, Japan
[3]*Physics Division, Argonne National Laboratory, Argonne, Illinois 60439, USA*

Abstract

A model for the $\bar{K}d \to \pi Y N$ reactions with $Y = \Lambda, \Sigma$ is developed, aiming at establishing the low-lying Λ and Σ hyperon resonances through analyzing the forthcoming data from the J-PARC E31 experiment. The off-shell amplitudes generated from the dynamical coupled-channels (DCC) model, which was developed in Phys. Rev. C **90**, 065204 (2014), are used as input to the calculations of the elementary $\bar{K}N \to \bar{K}N$ and $\bar{K}N \to \pi Y$ subprocesses in the $\bar{K}d \to \pi Y N$ reactions. It is shown that the cross sections for the J-PARC E31 experiment with a rather high incoming-$\bar{K}$ momentum, $|\vec{p}_{\bar{K}}| = 1$ GeV, can be predicted reliably only when the input $\bar{K}N \to \bar{K}N$ amplitudes are generated from a $\bar{K}N$ model, such as the DCC model used in this investigation, which describes the data of the $\bar{K}N$ reactions at energies far beyond the $\bar{K}N$ threshold. We find that the data of the threefold differential cross section $d\sigma/(dM_{\pi\Sigma}d\Omega_{p_n})$ for the $K^-d \to \pi\Sigma n$ reaction below the $\bar{K}N$ threshold can be used to test the predictions of the resonance poles associated with $\Lambda(1405)$. We also find that the momentum dependence of the threefold differential cross sections for the $K^-d \to \pi^-\Lambda p$ reaction can be used to examine the existence of a low-lying $J^P = 1/2^+$ Σ resonance with a pole mass $M_R = 1457 - i39$ MeV, which was found from analyzing the K^-p reaction data within the employed DCC model.

PACS numbers: 14.20.Jn, 13.75.Jz, 13.60.Le, 13.30.Eg

I. INTRODUCTION

Recently, the spectroscopic study of Λ and Σ hyperon resonances with strangeness $S = -1$ (collectively referred to as Y^*) has made significant progress. This advance mainly comes from using sophisticated coupled-channels approaches [1–4] to perform comprehensive partial-wave analyses of the existing data of K^-p reactions in a wide energy region from their thresholds to a rather high energy with the invariant mass $W = 2.1$ GeV. With this analysis, the systematic extraction of Y^* resonances defined by poles of the scattering amplitudes in the complex-energy plane was accomplished. It has been established [5] that the resonance poles can be identified with the (complex-)energy eigenstates of the Hamiltonian of the underlying fundamental theory, which are obtained under the purely outgoing wave boundary condition. Thus the Y^* resonance parameters extracted through the coupled-channels analyses of Refs. [1–4] have well defined theoretical meaning, while it is often not straightforward to interpret the Breit-Wigner parameters listed by Particle Data Group (PDG) [6]. In addition, attempts [7–9] are being made to develop methods for relating the meson and baryon resonance poles to the Lattice QCD calculations.

In this work, we consider the dynamical coupled-channels (DCC) model developed in Ref. [2] for the meson-baryon reactions in the $S = -1$ sector. This model was developed by extending the theoretical framework of Ref. [10], which was originally formulated to study πN, γN, eN, and νN reactions in the nucleon resonance region [11–24], to include the meson-baryon channels with strangeness $S = -1$. Within this DCC model, the T-matrix elements for each partial wave can be obtained by solving the following coupled integral equation [2]:

$$T_{\beta,\alpha}(p_\beta, p_\alpha; W) = V_{\beta,\alpha}(p_\beta, p_\alpha; W) + \sum_\delta \int p^2 dp V_{\beta,\delta}(p_\beta, p; W) G_\delta(p; W) T_{\delta,\alpha}(p, p_\alpha; W), \quad (1)$$

with

$$V_{\beta,\alpha}(p_\beta, p_\alpha; W) = v_{\beta,\alpha}(p_\beta, p_\alpha) + \sum_{Y^*_{0,n}} \frac{\Gamma^\dagger_{Y^*_{0,n},\beta}(p_\beta)\Gamma_{Y^*_{0,n},\alpha}(p_\alpha)}{W - M_{Y^*_{0,n}}}, \quad (2)$$

where W is the invariant mass of the reaction; the subscripts α, β, and δ represent the four two-body channels ($\bar{K}N$, $\pi\Sigma$, $\pi\Lambda$, $\eta\Lambda$, and $K\Xi$) and the two quasi-two-body channels ($\pi\Sigma^*$ and $\bar{K}^*N$) that can decay into the three-body $\pi\pi\Lambda$ and $\pi\bar{K}N$ channels, respectively; p_α is the magnitude of the momentum of channel α in the center-of-mass (CM) frame; G_δ is the Green's function of channel δ; $M_{Y^*_{0,n}}$ is the mass of the nth bare excited hyperon state $Y^*_{0,n}$ included in the given partial wave; $v_{\beta,\alpha}$ represents the hadron-exchange potentials derived from the effective Lagrangian that respects the SU(3) flavor symmetry; and the bare vertex interaction $\Gamma_{Y^*_{0,n},\alpha}$ ($\Gamma^\dagger_{Y^*_{0,n},\beta}$) defines the $\alpha \to Y^*_{0,n}$ ($Y^*_{0,n} \to \beta$) transition. The model parameters contained in the potential $V_{\beta,\alpha}$ were fixed by fitting more than 17,000 data of both unpolarized and polarized observables of the $K^-p \to \bar{K}N, \pi\Sigma, \pi\Lambda, \eta\Lambda, K\Xi$ reactions. As a result, we obtained two distinct sets of the model parameters, referred to as Model A and Model B. Both models describe the existing K^-p reaction data equally well over a wide energy range from the thresholds up to $W = 2.1$ GeV. From Model A (Model B), 18 (20) of Y^* resonances were extracted in the energy region above the $\bar{K}N$ threshold and below $W = 2.1$ GeV. It is found that some of the extracted low-lying Y^* resonances may correspond to one- and/or two-star resonances assigned by Particle Data Group [6] or may
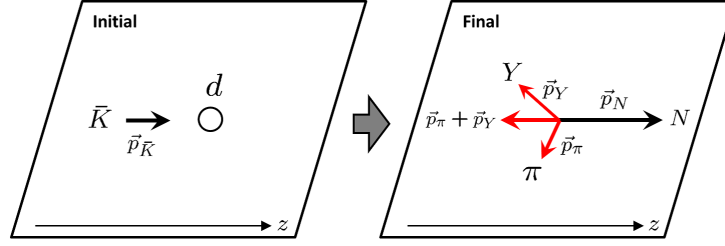
FIG. 1. Kinematics of the $\bar{K}d \to \pi YN$ reaction considered in this work. The outgoing N (outgoing πY-pair) momentum is in the direction (opposite direction) of the incoming-$\bar{K}$ momentum.
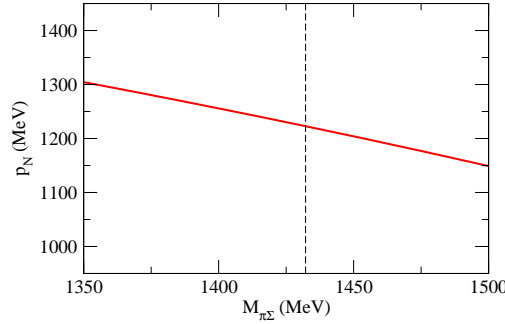

FIG. 2. The outgoing nucleon momentum $p_N \equiv |\vec{p}_N|$ (solid line) as function of the kinematically allowed πY invariant mass $M_{\pi Y}$ for the incoming-$\bar{K}$ momentum $|\vec{p}_{\bar{K}}| = 1$ GeV. Here the case that $Y = \Sigma$ is presented.

be new resonances. Furthermore, two $J^P = 1/2^-$ Λ resonances are found below the $\bar{K}N$ threshold in both Model A and Model B, which is similar to the results from the chiral unitary models (see, e.g., Refs. [25, 26]) and the Jülich model [27].

Although a number of new and/or unestablished low-lying Y^* resonances were found in the DCC analysis of Refs. [2, 3], their existence and pole-mass values are rather different between Model A and Model B. This is of course due to the fact that the existing K^-p reaction data used in the analysis are *incomplete*, as discussed in Refs. [2, 3]. In addition, there is a limitation of using the K^-p reaction data for establishing low-lying Y^* resonances because the K^-p reactions cannot directly access the energy region below the $\bar{K}N$ threshold, and also it is practically not easy to measure precisely the K^-p reactions in the energy region just above the $\bar{K}N$ threshold where the incoming-$\bar{K}$ momentum becomes very low. One of the most promising approaches to overcome this limitation would be a combined analysis of the K^-p reactions and the $K^-d \to \pi YN$ reactions. This is based on the observation that the two-body πY subsystem in the final state of the $K^-d \to \pi YN$ reactions can be in the energy region below the $\bar{K}N$ threshold even if the incoming-$\bar{K}$ momentum is rather high.

As a first step towards accomplishing such a combined analysis of the $\bar{K}N$ and $\bar{K}d$ reactions, in this work we apply the multiple scattering theory [28, 29] to predict the differential cross sections of the $\bar{K}d \to \pi YN$ reaction by using the $\bar{K}N$ reaction amplitudes generated from the DCC model of Ref. [2]. We focus on the kinematics that the incoming $\bar{K}$ has a rather high momentum of $|\vec{p}_{\bar{K}}| = 1$ GeV and the outgoing nucleon N is detected at very forward angles with $\theta_{p_N} \sim 0$, which is the same as the setup of the J-PARC E31 experiment [30]. At this special parallel kinematics, the outgoing N and the outgoing πY pair are
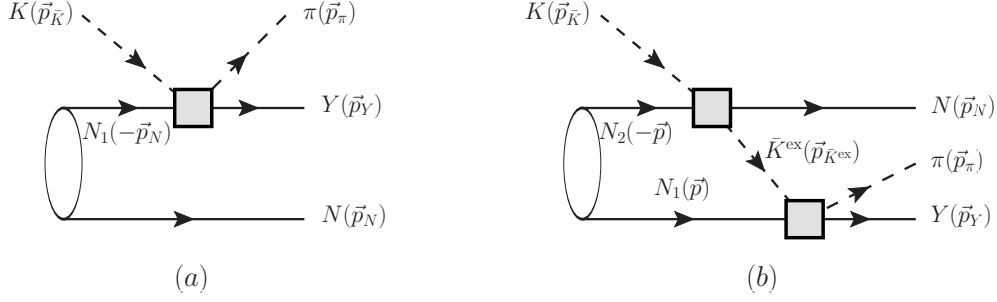
FIG. 3. Diagramatical representation of the $\bar{K}d \to \pi YN$ reaction processes considered in this work: (a) the impulse process; (b) the $\bar{K}$-exchange process. The deuteron wave function (open circles) is taken from the one constructed with the Argonne V18 potential [35], while the off-shell amplitudes describing the meson-baryon subprocesses (filled squares) are taken from our DCC model developed in Ref. [2].

scattered back-to-back, as illustrated in Fig. 1, and have almost no correlation in experimental measurements. In fact, as can be seen from Fig. 2, the forward moving nucleon momenta (solid curve) become $|\vec{p}_N| > |\vec{p}_K| = 1$ GeV for the invariant mass of the πY subsystem relevant to our study (horizontal axis), which means that the momentum of the πY pair is in an opposite direction to $\vec{p}_N$. Consequently, it is the best for examining Y^* resonances through their decays into πY states. In addition, since the forward moving nucleon carries high energy-momentum, the recoiled πY pair can be even below the $\bar{K}N$ threshold, which is also illustrated in Fig. 2. We thus can make predictions for investigating low-lying Y^* resonances, including the long-standing problem associated with $\Lambda(1405)$ that was also the focus of Refs. [31–34]. The data from the J-PARC E31 experiment [30] can then be used to test our results. In particular, we would like to examine how the predicted cross sections can be used to distinguish the resonance parameters extracted within Model A and Model B employed in our calculations.

Following the previous works [31–33] and justified by the special kinematics mentioned above, we assume that the scattering amplitude for $\bar{K}d \to \pi YN$ includes the single-scattering (impulse) term and the $\bar{K}$-exchange term, as illustrated in Fig. 3. While such a perturbative approach neglects the higher-order scattering processes in a recent calculation [34] based on the AGS-type of three-body scattering formulation [36], it is supported by many earlier studies of intermediate and high energy reactions on deuteron; see, for example, a recent study of $\gamma d \to \pi NN$ of Ref. [37]. Thus it is reasonable to assume that our results as well as the results of Refs. [31–33] account for the main features of the $\bar{K}d \to \pi YN$ reaction and can be used to explore the feasibility of using the experiment at J-PARC to investigate the low-lying hyperon resonances.

An essential difference between this work and the previous works [31–34] is that we employ the (off-shell) $\bar{K}N$ reaction amplitudes generated from the DCC model developed in Ref. [2]. This DCC model describes the $\bar{K}N$ reaction data over a very wide energy range from the thresholds up to $W = 2.1$ GeV. On the other hand, the models for the meson-baryon subprocesses employed in Refs. [31–34] were constructed by fitting only the K^-p reaction data just near the $\bar{K}N$ threshold. To see how these $\bar{K}N$ models can be used in the calculations, it is instructive here to examine the kinematics of the $\bar{K}$-exchange mechanism illustrated in Fig. 3(b). The range of the invariant mass of the outgoing πY system $(M_{\pi Y})$ we are interested in is $m_\pi + m_Y \leq M_{\pi Y} \lesssim 1.5$ GeV, where m_π (m_Y) is the mass of π
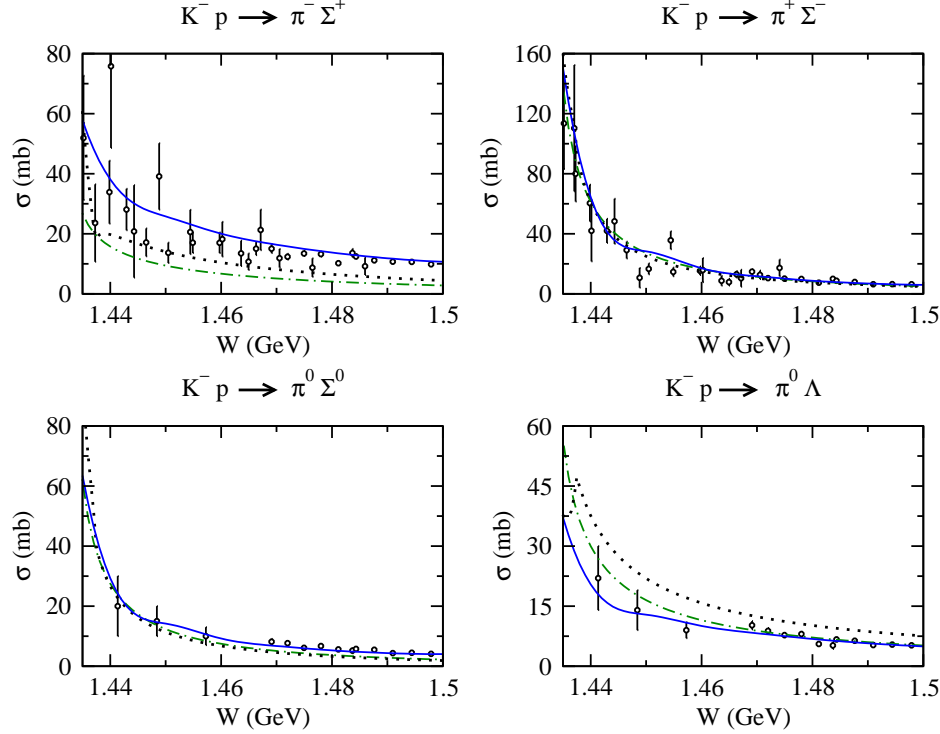
4

FIG. 4. Total cross sections for $K^-p \to \pi Y$ reactions near the threshold. Blue solid curves are Model B in Ref. [2], green dotted-dashed curves are the E-dep. model in Ref. [34], and black dotted curves are from the model developed in Ref. [38] that was used for the calculation in Refs. [31–33].

(Y). Thus the $\bar{K}^{\text{ex}}N_1 \to \pi Y$ amplitudes used for calculating the $\bar{K}$-exchange mechanism must be generated from models which can reproduce well the data near the $\bar{K}N$ threshold. As seen in Fig. 4, the models used in Refs. [31, 32, 34] and the DCC models employed in our calculations are all valid for this calculation in the invariant mass $M_{\pi Y}$ covered by the J-PARC E31 experiment shown in Fig. 2.

The situation is very different for the calculations of $\bar{K}N_2 \to \bar{K}^{\text{ex}}N$ amplitudes in Fig. 3(b). In the lower panel of Fig. 5, we show the ranges of the invariant mass $(W_{1\text{st}}^{\text{ex}})$ of the $\bar{K}N_2 \to \bar{K}^{\text{ex}}N$ subprocess, which can be formed from the incoming-$\bar{K}$ momentum $|\vec{p}_K| = 1$ GeV, the scattering angle of outgoing-N $\theta_{p_N} = 0$, and the momentum of initial nucleon N_2 with $|-\vec{p}| < 0.2$ GeV within which the deuteron wave function is large. We see that for a rather high incoming-$\bar{K}$ momentum with $|\vec{p}_K| = 1$ GeV, the allowed ranges for $W_{1\text{st}}^{\text{ex}}$ are in the well above the $\bar{K}N$ threshold region. In the upper panel of Fig. 5, we see that only the DCC model can describe the data in the whole range. Thus the models used in Refs. [31, 32, 34] have large uncertainties in calculating the $\bar{K}N_2 \to \bar{K}^{\text{ex}}N$ amplitudes for predicting $\bar{K}d \to \pi Y N$ at $|\vec{p}_{\bar{K}}| = 1$ GeV to compare with the data from the J-PARC E31 experiment [30]. In this work, we will also discuss how these uncertainties associated with the $\bar{K}N_2 \to \bar{K}^{\text{ex}}N$ amplitudes affect the resulting $\bar{K}d \to \pi Y N$ reactions cross sections.

In Sec. II, we first give the notations for kinematical variables and the cross section formulas necessary for the presentation of this work. We then give the formula for calculating the impulse and $\bar{K}$-exchange amplitudes of the $\bar{K}d \to \pi Y N$ reactions. The predicted results for the $\bar{K}d \to \pi Y N$ reaction from our model are presented in Sec. III. The comparisons with the results from using the S-wave $\bar{K}N$ models are also given there. A summary and
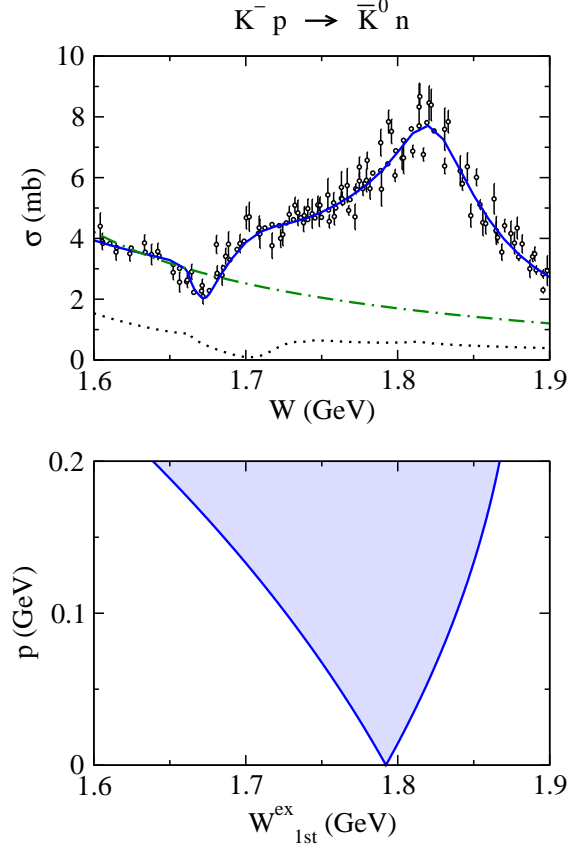
5

FIG. 5. Upper panel: Total cross section for $K^- p \to \bar{K}^0 n$ in the energy region relevant to the $\bar{K} N_2 \to \bar{K}^{\mathrm{ex}} N$ subprocess in the $\bar{K}$-exchange process [Fig. 3(b)]. Blue solid curve is Model B in Ref. [2], green dotted-dashed curve is the E-dep. model in Ref. [34], and black dotted curves is from the model developed in Ref. [38] that was used for the calculation in Refs. [31–33]. Lower panel: Allowed ranges of the invariant mass $W^{\mathrm{ex}}_{1\mathrm{st}}$ for the $\bar{K} N_2 \to \bar{K}^{\mathrm{ex}} N$ subprocess as $p \equiv |-\vec{p}|$ is varied. Here the incoming-$\bar{K}$ momentum and the scattering angle of outgoing N are fixed as $|\vec{p}_{\bar{K}}| = 1$ GeV and $\theta_{pN} = 0$, respectively.

the prospect for future works are given in Sec. IV.

II. FORMULATION

In this section, we present the formulas for the calculations of the differential cross sections for $\bar{K} + d \to \pi + Y + N$ that can be used to compare with the data from the J-PARC E31 experiment.

A. Kinematics and cross sections

We perform calculations in the laboratory (LAB) frame in which the incoming $\bar{K}$ is in the quantization z-direction and the outgoing N is on the x-z plane. The momenta for the

$\bar{K} + d \to \pi + Y + N$ reaction, denoted as p_a $(a = \bar{K}, d, \pi, Y, N)$, can then be written as

$$p_{\bar{K}} = (E_{\bar{K}}(\vec{p}_{\bar{K}}), 0, 0, |\vec{p}_{\bar{K}}|), \tag{3}$$

$$p_d = (m_d, \vec{0}), \tag{4}$$

$$p_\pi = (E_\pi(\vec{p}_\pi), \vec{p}_\pi), \tag{5}$$

$$p_Y = (E_Y(\vec{p}_Y), \vec{p}_Y), \tag{6}$$

$$p_N = (E_N(\vec{p}_N), |\vec{p}_N| \sin\theta_{p_N}, 0, |\vec{p}_N| \cos\theta_{p_N}), \tag{7}$$

where $E_a(\vec{p}_a) = (m_a^2 + \vec{p}_a^2)^{1/2}$ is the relativistic energy for a particle a with mass m_a and momentum $\vec{p}_a$. It is convenient to introduce the momentum $\vec{q}_\pi$ of the outgoing π in the center-of-mass (CM) frame of the final πY subsystem. For a given invariant mass $M_{\pi Y}$ of the πY subsystem, the magnitude of $\vec{q}_\pi$ is given by

$$|\vec{q}_\pi| = \frac{1}{2M_{\pi Y}} \sqrt{\lambda(M_{\pi Y}^2, m_\pi^2, m_Y^2)}, \tag{8}$$

where $\lambda(a, b, c)$ is the Källen function defined by $\lambda(a, b, c) = a^2 + b^2 + c^2 - 2ab - 2bc - 2ac$. For given $M_{\pi Y}$ and $\cos\theta_{p_N}$, $|\vec{p}_N|$ is obtained by solving $E_{\bar{K}}(\vec{p}_{\bar{K}}) + m_d = E_N(\vec{p}_N) + E_{\pi Y}$ where $E_{\pi Y} = \sqrt{M_{\pi Y}^2 + \vec{P}_{\pi Y}^2}$ and $\vec{P}_{\pi Y} \equiv \vec{p}_\pi + \vec{p}_Y = \vec{p}_{\bar{K}} - \vec{p}_N$. The momenta $\vec{p}_\pi$ for the outgoing π and $\vec{p}_Y$ for the outgoing Y can then be given by

$$\vec{p}_\pi = \vec{q}_\pi + \frac{\vec{P}_{\pi Y}}{M_{\pi Y}} \left[\frac{\vec{P}_{\pi Y} \cdot \vec{q}_\pi}{E_{\pi Y} + M_{\pi Y}} + E_\pi(\vec{q}_\pi) \right], \tag{9}$$

$$\vec{p}_Y = -\vec{q}_\pi + \frac{\vec{P}_{\pi Y}}{M_{\pi Y}} \left[-\frac{\vec{P}_{\pi Y} \cdot \vec{q}_\pi}{E_{\pi Y} + M_{\pi Y}} + E_Y(\vec{q}_\pi) \right], \tag{10}$$

With the above formulas, the kinematical variables [Eqs. (3)-(7)] are completely fixed by the incoming-$\bar{K}$ momentum $\vec{p}_{\bar{K}}$, the solid angle $\Omega_{p_N} = (\theta_{p_N}, \phi_{p_N} \equiv 0)$ of the outgoing N on the x-z plane, the solid angle $\Omega_{q_\pi} = (\theta_{q_\pi}, \phi_{q_\pi})$ of the outgoing π in the πY CM frame, and the πY invariant mass $M_{\pi Y}$.

With the normalization $\langle \vec{p}'|\vec{p}\rangle = \delta(\vec{p}' - \vec{p})$ for the plane-wave one-particle state, the unpolarized differential cross sections investigated in this work are given by

$$\frac{d\sigma}{dM_{\pi Y} d\Omega_{p_N}} = \int d\Omega_{q_\pi} \frac{d\sigma}{dM_{\pi Y} d\Omega_{p_N} d\Omega_{q_\pi}}, \tag{11}$$

$$\frac{d\sigma}{dM_{\pi Y} d\Omega_{p_N} d\Omega_{q_\pi}} = (2\pi)^4 \frac{E_{\bar{K}}(\vec{p}_{\bar{K}})}{|\vec{p}_{\bar{K}}|} \frac{E_\pi(\vec{p}_\pi) E_Y(\vec{p}_Y) E_N(\vec{p}_N) |\vec{q}_\pi| |\vec{p}_N|^2}{|[E_{\bar{K}}(\vec{p}_{\bar{K}}) + m_d] |\vec{p}_N| - E_N(\vec{p}_N) |\vec{p}_{\bar{K}}| \cos\theta_{p_N}|}$$
$$\times \frac{1}{(2J_d + 1)} \sum_{\text{spins}} |T_{\pi Y N, \bar{K} d}|^2, \tag{12}$$

where $d\Omega_p = d\phi_p d\cos\theta_p$; $J_d = 1$ is the spin of the deuteron; and $T_{\pi Y N, \bar{K} d}$ is the T-matrix element for the $\bar{K} d \to \pi Y N$ reaction.

B. Model for $\bar{K}d \to \pi YN$ reaction

As discussed in Sec. I, the cross section for the $\bar{K}d \to \pi YN$ reaction will be calculated from the mechanisms illustrated in Fig. 3. The T-matrix element $T_{\pi YN, \bar{K}d}$ appearing in Eq. (12) is given as a sum of contributions from the impulse ($T^{\text{imp}}_{\pi YN, \bar{K}d}$) and $\bar{K}$-exchange ($T^{\bar{K}\text{-ex}}_{\pi YN, \bar{K}d}$) processes:

$$T_{\pi YN, \bar{K}d} = T^{\text{imp}}_{\pi YN, \bar{K}d} + T^{\bar{K}\text{-ex}}_{\pi YN, \bar{K}d}. \tag{13}$$

The T-matrix element for the impulse process [Fig. 3(a)] is given by

$$T^{\text{imp}}_{\pi YN, \bar{K}d} = \sqrt{2}\langle \pi(\vec{p}_\pi, I^z_\pi); Y(\vec{p}_Y, S^z_Y, I^z_Y); N(\vec{p}_N, S^z_N, I^z_N)|t_{\pi Y, \bar{K}N_1}|\Psi^{(M_d)}_d; \bar{K}(\vec{p}_{\bar{K}}, I^z_{\bar{K}})\rangle$$

$$= \sqrt{2}\sum_{S^z_{N_1}} T_{\pi(I^z_\pi)Y(S^z_Y, I^z_Y), \bar{K}(I^z_{\bar{K}})N_1(S^z_{N_1}, -I^z_N)}(\vec{p}_\pi, \vec{p}_Y; \vec{p}_{\bar{K}}, -\vec{p}_N; W^{\text{imp}})$$

$$\times \Psi^{(M_d)}_d(-\vec{p}_N, S^z_{N_1}, -I^z_N; \vec{p}_N, S^z_N, I^z_N), \tag{14}$$

where I^z_a (S^z_a) is the quantum number for the z-component of the isospin I_a (the spin S_a) of the particle a; and M_d is that of the deuteron spin. The factor $\sqrt{2}$ comes from the antisymmetry property of the deuteron wave function given by the following standard form:

$$\Psi^{(M_d)}_d(\vec{p}, m_{s1}, m_{t1}; -\vec{p}, m_{s2}, m_{t2}) = (\tfrac{1}{2}m_{t1}, \tfrac{1}{2}m_{t2}|00)$$

$$\times \sum_{LM_LM_s} (LM_L, 1M_s|1M_d)(\tfrac{1}{2}m_{s1}, \tfrac{1}{2}m_{s2}|1M_s)$$

$$\times Y_{LM_L}(\hat{p})R_L(|\vec{p}|), \tag{15}$$

Here $(l_1m_1, l_2m_2|lm)$ is the Clebsch-Gordan coefficient for $l_1 \otimes l_2 \to l$; $Y_{LM}(\hat{p})$ is the spherical harmonics; and $R_L(|\vec{p}|)$ is the radial wave function. The radial wave function is normalized as

$$\sum_{L=0,2} \int_0^\infty p^2\, dp\, |R_L(p)|^2 = 1. \tag{16}$$

In this work, the radial wave function, $R_L(|\vec{p}|)$ with $L = 0, 2$, is taken from Ref. [35].

The half-off-shell $\bar{K}N_1 \to \pi Y$ scattering in Eq. (14) can be related to the one in its CM frame by

$$T_{\pi(I^z_\pi)Y(S^z_Y, I^z_Y), \bar{K}(I^z_{\bar{K}})N_1(S^z_{N_1}, -I^z_N)}(\vec{p}_\pi, \vec{p}_Y; \vec{p}_{\bar{K}}, -\vec{p}_N; W^{\text{imp}}) =$$

$$\sqrt{\frac{E_\pi(\vec{q}_\pi)E_Y(-\vec{q}_\pi)E_{\bar{K}}(\vec{q}_{\bar{K}})E_N(-\vec{q}_{\bar{K}})}{E_\pi(\vec{p}_\pi)E_Y(\vec{p}_Y)E_{\bar{K}}(\vec{p}_{\bar{K}})E_N(-\vec{p}_N)}} T^{\text{CM}}_{\pi(I^z_\pi)Y(S^z_Y, I^z_Y), \bar{K}(I^z_{\bar{K}})N_1(S^z_{N_1}, -I^z_N)}(\vec{q}_\pi, -\vec{q}_\pi; \vec{q}_{\bar{K}}, -\vec{q}_{\bar{K}}; W^{\text{imp}}), \tag{17}$$

where $\vec{q}_{\bar{K}}$ is the momentum of the incoming $\bar{K}$ in the CM frame of the final πY system; the Lorentz-boost factor appears in the right hand side[1]; and the invariant mass W^{imp} for the $\bar{K}N_1 \to \pi Y$ subprocess is defined by

$$W^{\text{imp}} = M_{\pi Y}. \tag{18}$$

---

[1] Strictly speaking, the Wigner rotations also take place for the particle spins through the Lorentz boost. However, those are omitted here because those do not affect the unpolarized differential cross sections considered in this work.

Furthermore, the partial-wave expansion of the amplitude in the CM frame is expressed as

$$T^{\mathrm{CM}}_{\pi(I^z_\pi)Y(S^z_Y,I^z_Y),\bar{K}(I^z_{\bar{K}})N_1(S^z_{N_1},-I^z_N)}(\vec{q}_\pi,-\vec{q}_\pi;\vec{q}_{\bar{K}},-\vec{q}_{\bar{K}};W^{\mathrm{imp}}) =$$

$$\sum_{JLJ^zL^z_fL^z_i}\sum_{II^z} Y_{LL^z_f}(\hat{q}_f)Y^*_{LL^z_i}(\hat{q}_i)(LL^z_f,S_YS^z_Y|JJ^z)(LL^z_i,S_{N_1}S^z_{N_1}|JJ^z)$$

$$\times (I_\pi I^z_\pi, I_Y I^z_Y|II^z)(I_{\bar{K}}I^z_{\bar{K}},I_{N_1}-I^z_N|II^z)\, T^{(IJL)}_{\pi Y,\bar{K}N_1}(q_\pi,q_{\bar{K}};W^{\mathrm{imp}}),\quad (19)$$

As already mentioned, in this work we take the partial-wave amplitudes $T^{(IJL)}_{\pi Y,\bar{K}N_1}(q_\pi,q_{\bar{K}};W^{\mathrm{imp}})$ from the DCC model developed in Ref. [2].

For the $\bar{K}$-exchange process [Fig. 3(b)], the corresponding T-matrix element is expressed as

$$T^{\bar{K}\text{-ex}}_{\pi YN,\bar{K}d} = \sqrt{2}\langle\pi(\vec{p}_\pi,I^z_\pi);Y(\vec{p}_Y,S^z_Y,I^z_Y);N(\vec{p}_N,S^z_N,I^z_N)|$$

$$\times\hat{t}_{\pi Y,\bar{K}^{\text{ex}}N_1}\hat{G}_{\bar{K}^{\text{ex}}NN_1}\hat{t}_{\bar{K}^{\text{ex}}N,\bar{K}N_2}|\Psi^{(M_d)}_d;\bar{K}(\vec{p}_{\bar{K}},I^z_{\bar{K}})\rangle$$

$$=\sum_{S^z_{N_1}S^z_{N_2}}\sum_{I^z_{\bar{K}^{\text{ex}}}I^z_{N_1}I^z_{N_2}}\int d\vec{p}_{\bar{K}^{\text{ex}}}$$

$$\times T_{\pi(I^z_\pi)Y(S^z_Y,I^z_Y),\bar{K}^{\text{ex}}(I^z_{\bar{K}^{\text{ex}}})N_1(S^z_{N_1},I^z_{N_1})}(\vec{p}_\pi,\vec{p}_Y;\vec{p}_{\bar{K}^{\text{ex}}},\vec{p};W^{\text{ex}}_{\text{2nd}})$$

$$\times\frac{1}{E-E_{\bar{K}^{\text{ex}}}(\vec{p}_{\bar{K}^{\text{ex}}})-E_N(\vec{p}_N)-E_{N_1}(\vec{p})+i\varepsilon}$$

$$\times T_{\bar{K}^{\text{ex}}(I^z_{\bar{K}^{\text{ex}}})N(S^z_N,I^z_N),\bar{K}(I^z_{\bar{K}})N_2(S^z_{N_2},I^z_{N_2})}(\vec{p}_{\bar{K}^{\text{ex}}},\vec{p}_N;\vec{p}_{\bar{K}},-\vec{p};W^{\text{ex}}_{\text{1st}})$$

$$\times\Psi^{(M_d)}_d(\vec{p},S^z_{N_1},I^z_{N_1};-\vec{p},S^z_{N_2},I^z_{N_2}),\quad (20)$$

where $\vec{p}=\vec{p}_\pi+\vec{p}_Y-\vec{p}_{\bar{K}^{\text{ex}}}=\vec{p}_{\bar{K}}-\vec{p}_N-\vec{p}_{\bar{K}^{\text{ex}}}$; and E is the total scattering energy in the LAB frame. $W^{\text{ex}}_{\text{1st}}$ and $W^{\text{ex}}_{\text{2nd}}$ are respectively the invariant mass for the $\bar{K}N_2\to\bar{K}^{\text{ex}}N$ and $\bar{K}^{\text{ex}}N_1\to\pi Y$ subprocesses that describe the first and second meson-baryon interaction vertices [filled squares in Fig. 3(b)] in the $\bar{K}$-exchange process. The explicit form of $W^{\text{ex}}_{\text{1st}}$ and $W^{\text{ex}}_{\text{2nd}}$ are given by

$$W^{\text{ex}}_{\text{1st}} = \sqrt{[E_{\bar{K}}(\vec{p}_{\bar{K}})+m_d-E_{N_1}(\vec{p})]^2-(\vec{p}_N+\vec{p}_{\bar{K}^{\text{ex}}})^2},\quad (21)$$

$$W^{\text{ex}}_{\text{2nd}} = M_{\pi Y}.\quad (22)$$

Again, the off-shell plane-wave amplitude for the $\bar{K}N_2\to\bar{K}^{\text{ex}}N$ and $\bar{K}^{\text{ex}}N_1\to\pi Y$ subprocesses are constructed with the partial-wave amplitudes generated from the DCC model [2] in a way similar to Eqs. (17) and (19).

III.   RESULTS AND DISCUSSION

With the model described in the previous section, we can use Eqs. (11) and (12) to calculate the differential cross sections for the $K^-d\to\pi YN$ reactions. We will first present our predictions for using the forthcoming data from the J-PARC E31 experiment to examine the low-lying Y^* resonances that were extracted [3] from the two DCC models, Model A and Model B, of Ref. [2]. We then discuss the differences between our results with those given in Refs. [31, 32, 34].
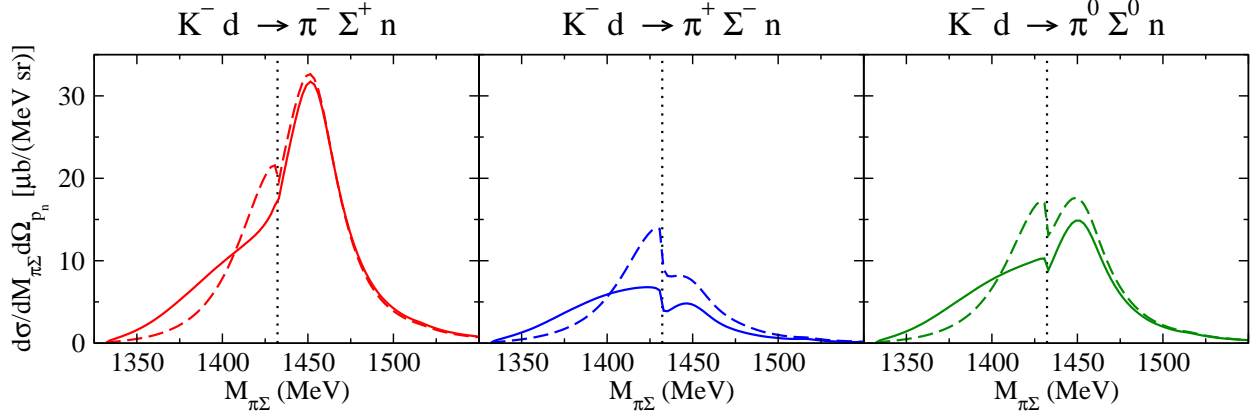
9

FIG. 6. Threefold differential cross section $d\sigma/(dM_{\pi\Sigma}d\Omega_{p_n})$ for the $K^-d \to \pi\Sigma n$ reactions at $|\vec{p}_{K^-}| = 1$ GeV and $\theta_{p_n} = 0$. Solid curves (dashed curves) are the full results for which the off-shell partial-wave amplitudes of Model A (Model B) of our DCC model [2] are used for the two-body meson-baryon subprocesses. Dotted vertical lines indicate the $\pi\Sigma$ invariant mass at the $\bar{K}N$ threshold.

A. Predictions for J-PARC E31 experiment

To make predictions for the J-PARC E31 experiment, we consider the kinematics that the momentum of the incoming K^- is set as $|\vec{p}_{K^-}| = 1$ GeV and the momentum of the outgoing N is chosen to be in the K^- direction with $\theta_{p_N} = 0$. We perform calculations using the $\bar{K}N \to \bar{K}N$ and $\bar{K}N \to \pi Y$ amplitudes generated from both of the DCC models (Model A and Model B) constructed in Ref. [2]. The predicted K^-d results are denoted as Model A and Model B accordingly.

First of all, we observe that the impulse process [Fig. 3(a)] gives negligible contribution at the considered kinematics with $|\vec{p}_{K^-}| = 1$ GeV and $\theta_{p_N} = 0$, and the cross sections are completely dominated by the $\bar{K}$-exchange process [Fig. 3(b)]. This is expected since the impulse amplitude (14) contains the deuteron wave function $\Psi_d(-\vec{p}_N, \vec{p}_N)$, which becomes very small in the considered kinematics where the momentum $\vec{p}_N$ is very high, $|\vec{p}_N| \sim 1.2$ GeV, as indicated in Fig. 2. Therefore, in the following, our discussions are focused on the $\bar{K}$-exchange process.

Figure 6 shows the predicted threefold differential cross section $d\sigma/(dM_{\pi\Sigma}d\Omega_n)$ for the $K^-d \to \pi\Sigma n$ reactions. There are two noticeable features. First, there is a significant enhancement of the cross section at $M_{\pi\Sigma} \sim 1.45$ GeV. Second, a varying structure, partly due to the cusp from the opening of the $\bar{K}N$ channel, appears in the considered $M_{\pi\Sigma}$ region, and its shape depends on the model and the charge state of the final $\pi\Sigma$ system. We analyze their origins in the following.

The enhancement of the cross section in Fig. 6 at $M_{\pi\Sigma} \sim 1.45$ GeV is mainly due to the fact that the meson-baryon amplitudes are in general the largest at the on-shell kinematics and the deuteron wave function $\Psi_d(\vec{p}, -\vec{p})$ is the largest at $|\vec{p}| = 0$. At $M_{\pi\Sigma} \sim 1.45$ GeV, all of the meson-baryon subprocesses and three-body propagator in the $\bar{K}$-exchange process become almost on-shell when the momenta of the nucleons inside the deuteron are near $|\vec{p}| = 0$ in the integrand of Eq. (20). Thus the magnitude of $\bar{K}$-exchange amplitude $|T_{\pi Y N, \bar{K}d}^{\bar{K}-\text{ex}}|$ gets a large enhancement at $M_{\pi\Sigma} \sim 1.45$ GeV. This is similar to what was discussed in Ref. [34]. In fact, we confirm that the enhancement disappears if we omit the contribution
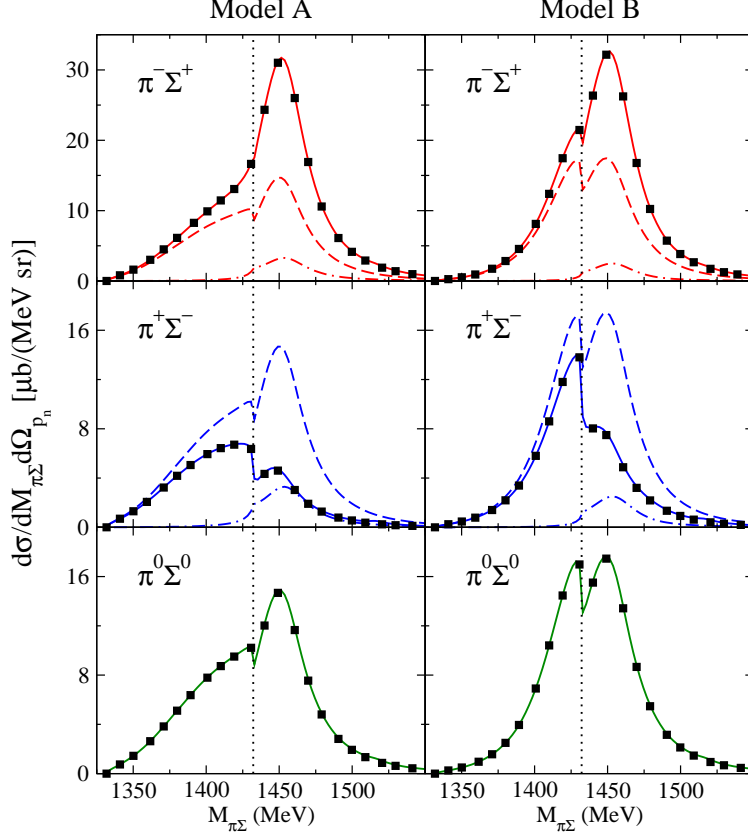
10

FIG. 7. Threefold differential cross section $d\sigma/(dM_{\pi\Sigma}d\Omega_{p_n})$ for the $K^-d \to \pi\Sigma n$ reactions with $|\vec{p}_{K^-}| = 1$ GeV and $\theta_{p_n} = 0$. Top, middle, and bottom panels are the results for $K^-d \to \pi^-\Sigma^+n$, $K^-d \to \pi^+\Sigma^-n$, and $K^-d \to \pi^0\Sigma^0n$, respectively. The results from Model A (Model B) are presented in left panels (right panels). Each of curves and points is: the full results (solid curves); the results in which only the S-wave amplitude (filled squares), the S_{01} amplitude (dashed curves), or the S_{11} amplitude (dashed-dotted curves) is included in $\bar{K}^{\rm ex}N_1 \to \pi\Sigma$ of the $\bar{K}$-exchange process. Dotted vertical lines indicate the $\pi\Sigma$ invariant mass at the $\bar{K}N$ threshold.

232 from the $|\vec{p}| < 0.2$ GeV region in the loop integration in Eq. (20).

233   We now examine the varying structure of $d\sigma/(dM_{\pi\Sigma}d\Omega_{p_n})$ in Fig. 6. For this purpose,
234 we first observe in Fig. 7 that the results (filled squares) from keeping only the S wave
235 of the $\bar{K}^{\rm ex}N_1 \to \pi\Sigma$ amplitude agree almost perfectly with the full results (solid curves).
236 This indicates that the $\bar{K}^{\rm ex}N_1 \to \pi\Sigma$ subprocess is completely dominated by the S-wave
237 amplitudes in the considered kinematics. We note that this explains why a peak due to the
238 $\Lambda(1520)3/2^-$ resonance does not appear at $M_{\pi\Sigma} \sim 1.52$ GeV in contrast to the case of the
239 K^-p reactions. In the same figure, we also show the contributions from S_{01} (dashed curves)
240 and S_{11} (dashed-dotted curves) partial waves[2] of the $\bar{K}^{\rm ex}N_1 \to \pi\Sigma$ subprocess. Clearly, the
241 main contributions to the full results (solid curves) are from the S_{01} wave that show the
242 clear cusp structure near the $\bar{K}N$ threshold. However, their interference with the S_{11} wave
243 is significant and is constructive (destructive) for the $\pi^-\Sigma^+$ ($\pi^+\Sigma^-$) production reactions.
244 Such interference is absent for the $\pi^0\Sigma^0$ production reaction, since only the S_{01} wave of the

---

[2] The partial wave of the two-body $\bar{K} + N \to M(0^-) + B(\frac{1}{2}^+)$ reactions is denoted as L_{I2J}, which means that the partial wave has a total angular momentum J, a total isospin I, and a parity $P = (-)^L$.
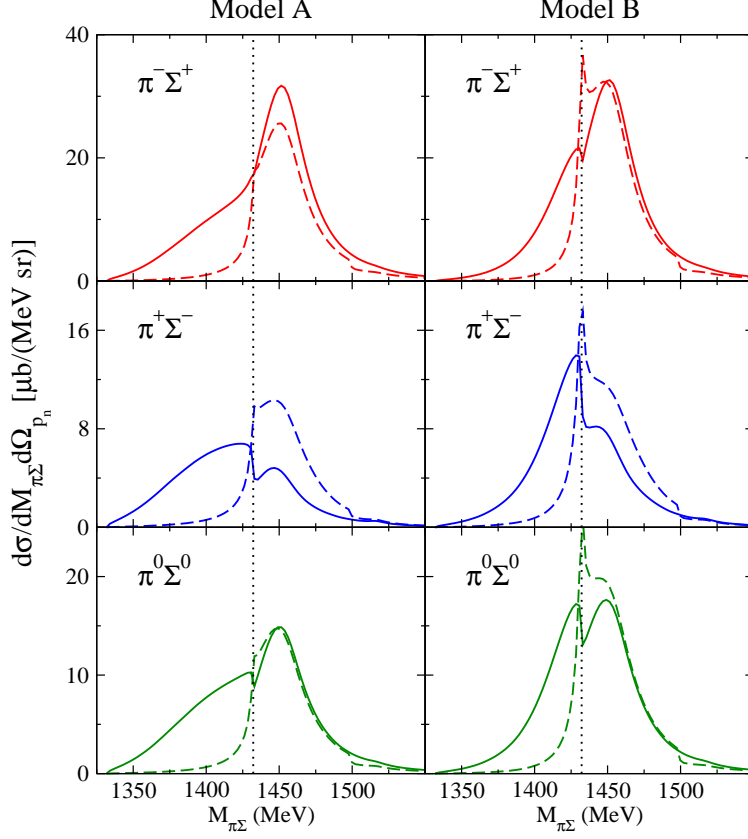
FIG. 8. Threefold differential cross section $d\sigma/(dM_{\pi\Sigma}d\Omega_{p_n})$ for the $K^-d \to \pi\Sigma n$ reactions with $|\vec{p}_{K^-}| = 1$ GeV and $\theta_{p_n} = 0$. Top, middle, and bottom panels are the results for $K^-d \to \pi^-\Sigma^+n$, $K^-d \to \pi^+\Sigma^-n$, and $K^-d \to \pi^0\Sigma^0 n$, respectively. The results from Model A (Model B) are presented in left panels (right panels). Solid curves are the full results, while dashed curves are the same as solid curves except that only the nonresonant contribution is included for the S_{01} amplitude of the $\bar{K}^{\mathrm{ex}}N_1 \to \pi\Sigma$ subprocess. Dotted vertical lines indicate the $\pi\Sigma$ invariant mass at the $\bar{K}N$ threshold.

245    $\bar{K}^{\mathrm{ex}}N_1 \to \pi\Sigma$ subprocess can contribute to the cross section.

246   We next examine how the characteristic differences between Model A and Model B in the
247 shape of the cross sections below the $\bar{K}N$ threshold (compare solid and dashed curves in
248 Fig. 6) can be related to resonances in the S_{01} partial wave of the $\bar{K}^{\mathrm{ex}}N_1 \to \pi\Sigma$ subprocess.
249 For this purpose, we first observe in Fig. 8 that the cross sections become very small below
250 the $\bar{K}N$ threshold if we take into account only the nonresonant contribution for the S_{01}
251 wave of $\bar{K}^{\mathrm{ex}}N_1 \to \pi\Sigma$. With this observation, we expect that S_{01} $(J^P = 1/2^-)$ Λ resonances
252 are actually the main contribution of the cross sections below the $\bar{K}N$ threshold and are
253 the origin of the difference in its shape between Model A and Model B. As mentioned in
254 Sec. I, our DCC analysis of the K^-p reactions [2] predicts two S_{01} $(J^P = 1/2^-)$ Λ resonances
255 below the $\bar{K}N$ threshold in both Model A and Model B [3], as shown in Fig. 9. Here, the
256 higher mass pole (A1 and B1) would correspond to the $\Lambda(1405)$ resonance, while another Λ
257 resonance with lower mass (A2 and B2) is similar to what was obtained in the chiral unitary
258 models (see, e.g., Ref. [26]) and the Jülich model [27]. Although both Model A and Model
259 B find two Λ resonances, their pole positions are rather different. One can see from Fig. 9
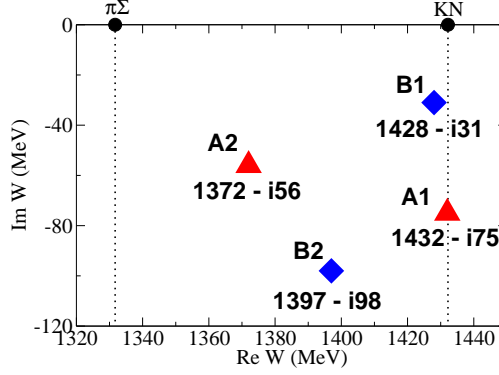
12

FIG. 9. Pole positions of S_{01} ($J^P = 1/2^-$) Λ resonances located below the $\bar{K}N$ threshold [3], which were extracted within the DCC models developed in Ref. [2]. Red triangles (blue diamonds) are the resonance pole positions obtained from Model A (Model B).

TABLE I. The product of coupling strengths $g_{\pi\Sigma Y^*} g_{\bar{K}N Y^*}$ at pole positions for $J^P = 1/2^-$ Λ resonances located below the $\bar{K}N$ threshold. The pole mass M_R is presented as $(\mathrm{Re}(M_R), -\mathrm{Im}(M_R))$, and $g_{\pi\Sigma Y^*} g_{\bar{K}N Y^*} = |g_{\pi\Sigma Y^*} g_{\bar{K}N Y^*}| e^{i\phi}$ is presented as $(|g_{\pi\Sigma Y^*} g_{\bar{K}N Y^*}|, \phi)$. The product $g_{\pi\Sigma Y^*} g_{\bar{K}N Y^*}$ is defined as the residue of the T-matrix element $T_{\pi\Sigma, \bar{K}N}$ at the resonance pole position.

	Pole mass M_R (MeV)	$g_{\pi\Sigma Y^*} g_{\bar{K}N Y^*}$ (MeV^{-1}, deg.)	$|g_{\pi\Sigma Y^*} g_{\bar{K}N Y^*}/\mathrm{Im}(M_R)|^2$ (MeV^{-4})
A1	$(1432, 75)$	$(15.42 \times 10^{-4}, 170)$	4.23×10^{-10}
B1	$(1428, 31)$	$(7.94 \times 10^{-4}, 102)$	6.56×10^{-10}
A2	$(1372, 56)$	$(21.54 \times 10^{-4}, -24)$	14.79×10^{-10}
B2	$(1397, 98)$	$(13.87 \times 10^{-4}, -56)$	2.00×10^{-10}

that the pole A1 (B2) has larger imaginary part than the pole B1 (A2) and is far away from the real energy axis. In addition, the products of their coupling strengths to the $\pi\Sigma$ and $\bar{K}N$ channels, $g_{\pi\Sigma Y^*} \times g_{\bar{K}N Y^*}$, are rather different as seen in Table I. The contribution of a resonance with complex mass M_R in the $\bar{K}^{\mathrm{ex}} N_1 \to \pi\Sigma$ subprocess to the $\bar{K}$-exchange amplitude $T_{\pi\Sigma n, K^- d}^{\bar{K}\text{-ex}}$ can be schematically expressed at $M_{\pi\Sigma} = \mathrm{Re}(M_R)$ as

$$
\begin{aligned}
T_{\pi\Sigma n, K^- d}^{\bar{K}\text{-ex}} &\sim \left[F(M_{\pi\Sigma}) \times \frac{g_{\pi\Sigma Y^*} g_{\bar{K}N Y^*}}{M_{\pi\Sigma} - M_R} + \cdots \right]_{M_{\pi\Sigma} = \mathrm{Re}(M_R)} \\
&= F\big(\mathrm{Re}(M_R)\big) \times \frac{g_{\pi\Sigma Y^*} g_{\bar{K}N Y^*}}{i\,\mathrm{Im}(M_R)} + \cdots,
\end{aligned}
\tag{23}
$$

where $F(M_{\pi\Sigma})$ is a regular function of $M_{\pi\Sigma}$ and is expected not to be much different between Model A and Model B. The value of $|g_{\pi\Sigma Y^*} g_{\bar{K}N Y^*}/\mathrm{Im}(M_R)|^2$ can therefore be used to measure the effect of a resonance on the cross section. In the third column of Table I, we see that $|g_{\pi\Sigma Y^*} g_{\bar{K}N Y^*}/\mathrm{Im}(M_R)|^2$ of the resonance B1 is larger than that of A1. Thus B1 has larger effects than A1 on the cross sections near the $\bar{K}N$ threshold, as can be seen from clear peaks in the cross sections at $M_{\pi\Sigma} \sim 1.42$ GeV that appear only in Model B. At lower energy, the cross sections are influenced by the second resonances A2 and B2. From Table I, we see that $|g_{\pi\Sigma Y^*} g_{\bar{K}N Y^*}/\mathrm{Im}(M_R)|^2$ of the resonance A2 is much larger that that of B2. This explains
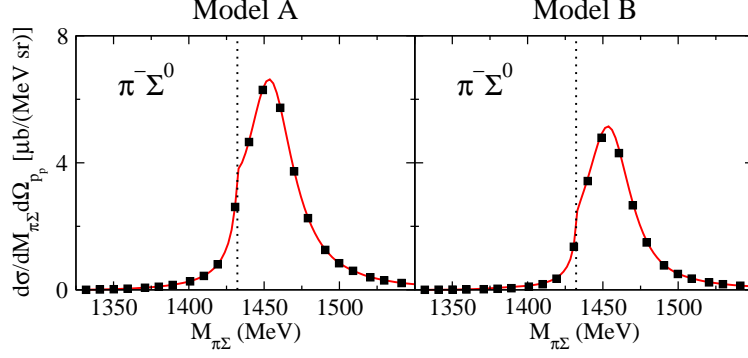
13

FIG. 10. Threefold differential cross section $d\sigma/(dM_{\pi\Sigma}d\Omega_{p_p})$ for the $K^-d \to \pi^-\Sigma^0 p$ reaction at $|\vec{p}_{K^-}| = 1$ GeV and $\theta_{p_p} = 0$. The results from Model A (Model B) are presented in the left panel (right panel). Solid curves are the full results, while filled squares are the results in which only the S_{11} amplitude is included for $\bar{K}^{ex}N_1 \to \pi\Sigma$ of the $\bar{K}$-exchange process. Dotted vertical lines indicate the $\pi\Sigma$ invariant mass at the $\bar{K}N$ threshold.
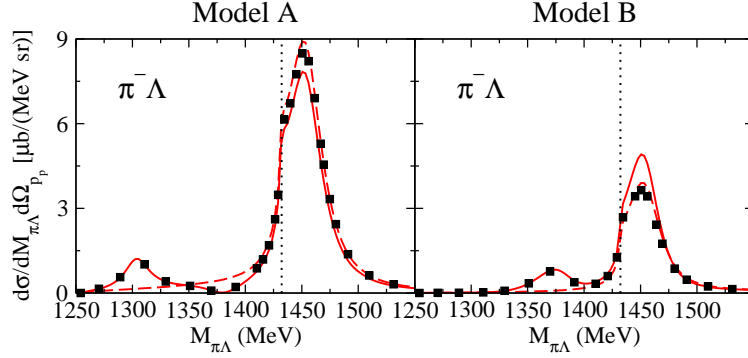

FIG. 11. Threefold differential cross section $d\sigma/(dM_{\pi\Lambda}d\Omega_{p_p})$ for the $K^-d \to \pi^-\Lambda p$ reaction at $|\vec{p}_{K^-}| = 1$ GeV and $\theta_{p_p} = 0$. The results from Model A (Model B) are presented in the left panel (right panel). Each of curves and points is: the full results (solid curves); the results in which only the S_{11} amplitude (dashed curves) or the S_{11} and P_{13} amplitudes (filled squares) is included for $\bar{K}^{ex}N_1 \to \pi\Lambda$ of the $\bar{K}$-exchange process. Dotted vertical lines indicate the $\pi\Lambda$ invariant mass at the $\bar{K}N$ threshold.

why the cross sections at $M_{\pi\Sigma} \lesssim 1.4$ GeV in Model A are larger than Model B.

We now turn to presenting the predicted cross sections for $K^-d \to \pi^-\Sigma^0 p$ and $K^-d \to \pi^-\Lambda p$ at the same kinematics $|\vec{p}_{\bar{K}}| = 1$ GeV and $\theta_{p_p} = 0$. Since the $\pi^-\Sigma^0$ and $\pi^-\Lambda$ states contain only the isospin $I = 1$ component, these reactions will be useful for investigating the low-lying Σ resonances. It is noted that the data for such reactions can also be obtained by extending the measurements of the the J-PARC E31 experiment [39]. Similar to the results for the $K^-d \to \pi\Sigma n$ reactions presented above, we find that (a) the impulse process gives negligible contribution to the cross sections for both $K^-d \to \pi^-\Sigma^0 p$ and $K^-d \to \pi^-\Lambda p$, and (b) the characteristic enhancement appears at $M_{\pi Y} \sim 1.45$ GeV as seen in Figs. 10 and 11.

For $K^-d \to \pi^-\Sigma^0 p$, we find that the $\bar{K}^{ex}N_1 \to \pi\Sigma$ subprocess is completely dominated by the S_{11} amplitude. This is shown in Fig. 10. We see that the results (filled squares) from the calculations keeping only the S_{11} amplitude of the $\bar{K}^{ex}N_1 \to \pi\Sigma$ subprocess agree almost perfectly with the results (solid curves) from the calculations including all partial

14

waves. The cross section becomes very small below the $\bar{K}N$ threshold, and this would be because no resonance exists in the S_{11} wave in the corresponding energy region. It is found that Model B shows the cross section $\sim 20\,\%$ smaller than Model A at its maximum ($M_{\pi\Sigma} \sim 1.45$ GeV). Since the on-shell S_{11} amplitudes for the $\bar{K}^{\mathrm{ex}}N_1 \to \pi\Sigma$ subprocess are not much different between the two models at $M_{\pi\Sigma} \sim 1.45$ GeV [2], the difference in the magnitude of the $K^-d \to \pi^-\Sigma^0 p$ cross section might partly come from that in the off-shell behavior of the $\bar{K}^{\mathrm{ex}}N_1 \to \pi\Sigma$ subprocess.

The predicted differential cross sections for the $K^-d \to \pi^-\Lambda p$ reaction are given in Fig. 11. By comparing the solid and filled squares, it is clear that the S_{11} and P_{13} waves of the $\bar{K}^{\mathrm{ex}}N_1 \to \pi\Lambda$ subprocess completely dominate the cross section in the region below the $\bar{K}N$ threshold. A resonance corresponding to $\Sigma(1385)3/2^+$ in the P_{13} wave was identified in both Model A and Model B. For Model B (the right panel of Fig. 11), there is a peak at $M_{\pi\Lambda} \sim 1.38$ GeV, where the contribution from the S_{11} amplitude is very weak. On the other hand, we find that in Model A the S_{11}-wave contribution and the P_{13}-wave contribution from $\Sigma(1385)3/2^+$ are comparable and interfere destructively, and, as a result, a dip is produced at $M_{\pi\Lambda} \sim 1.38$ GeV. We find that Model A has another P_{13} resonance with lower mass than $\Sigma(1385)3/2^+$. This is the origin of the peak at $M_{\pi\Lambda} \sim 1.3$ GeV in the left panel of Fig. 11. These kinds of visible differences between Model A and Model B can occur below the $\bar{K}N$ threshold, because at present our DCC models for the $\bar{K}N$ reactions have been constructed by fitting only to the K^-p reaction data. We expect that such a different behavior of the two-body subprocesses below the $\bar{K}N$ threshold, which cannot be directly constrained by the $\bar{K}N$ reaction data, needs to be judged by the data of $\bar{K}d$ reactions. The upcoming data from the J-PARC E31 experiment are thus highly desirable to improve our DCC models in the $S = -1$ sector.

We also see in Fig. 11 that above the $\bar{K}N$ threshold, the P_{13} wave of the $\bar{K}^{\mathrm{ex}}N_1 \to \pi\Lambda$ subprocess is negligible and the main contribution to the cross section comes from the S_{11} wave. However, the behavior of the S_{11} partial-wave amplitudes for $\bar{K}N \to \pi\Lambda$ is rather different between Model A and Model B at $W \lesssim 1.7$ GeV (see Fig. 27 in Ref. [2]), and this is the origin of the the sizable difference in the magnitude of the cross section above the $\bar{K}N$ threshold. For Model A (left panel), the difference between the solid and dashed curves are quite small, and hence the cross section above the $\bar{K}N$ threshold is almost completely dominated by the S_{11} wave. On the other hand, this difference is about $30\,\%$ for Model B (right panel) and is found to come from a P_{11} ($J^P = 1/2^+$) Σ resonance with pole mass $M_R = 1457 - i39$ MeV [3]. This resonance might correspond to the one-star $\Sigma(1480)$ resonance assigned by PDG [6]. At present this resonance was found only in Model B, and this is why the contribution of P_{11} wave is negligible in the $K^-d \to \pi^-\Lambda p$ cross section for Model A.

The above result suggests that the $K^-d \to \pi^-\Lambda p$ cross section may provide a useful constraint for judging this unestablished low-lying Σ resonance with spin-parity $J^P = 1/2^+$. To investigate this, we examine the threefold differential cross sections at different values of the incoming-$\bar{K}$ momentum. In Fig. 12, we present $d\sigma/(dM_{\pi\Lambda}d\Omega_{p_p})$ at $|\vec{p}_{\bar{K}}| = 1$ GeV and 0.7 GeV. We find that the interference pattern in the cross section changes as $|\vec{p}_{\bar{K}}|$ changes. For the cross section at $|\vec{p}_{\bar{K}}| = 1$ GeV, the contribution from the P_{11} wave of the $\bar{K}^{\mathrm{ex}}N_1 \to \pi\Lambda$ subprocess shows a constructive interference with the other contributions, while at $|\vec{p}_{\bar{K}}| = 0.7$ GeV, it shows a destructive interference. This visible difference of the interference pattern originating from the P_{11} wave of the $\bar{K}^{\mathrm{ex}}N_1 \to \pi\Lambda$ subprocess will provide critical information for judging the unestablished $J^P = 1/2^+$ Σ resonance. Therefore
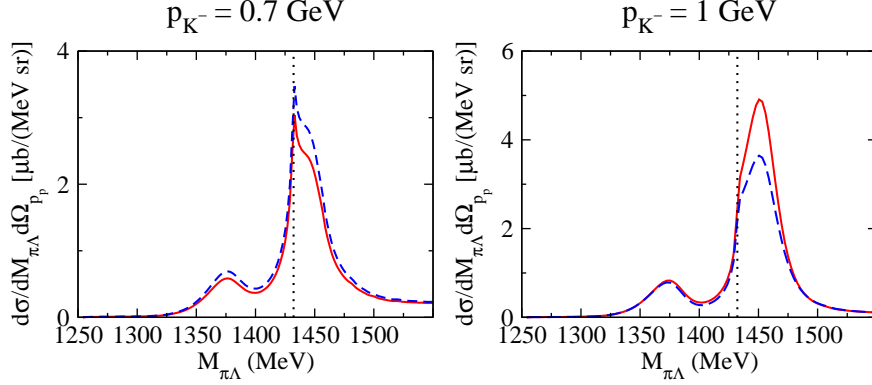
15

FIG. 12. Threefold differential cross section $d\sigma/(dM_{\pi\Lambda}d\Omega_{p_p})$ for the $K^-d \to \pi^-\Lambda p$ reaction at $\theta_{p_p} = 0$, computed with Model B. The left (right) panel is the result at $|\vec{p}_{\bar{K}}| = 0.7$ GeV ($|\vec{p}_{\bar{K}}| = 1$ GeV). Solid curves are the full results, while dashed curves are the results in which the P_{11} amplitude for $\bar{K}^{ex}N_1 \to \pi\Lambda$ in the $\bar{K}$-exchange process is turned off. Dotted vertical lines indicate the $\pi\Lambda$ invariant mass at the $\bar{K}N$ threshold.

it is highly desirable to measure the $K^-d \to \pi^-\Lambda p$ cross section for several $|\vec{p}_{\bar{K}}|$ values.

B. Comparison with the results from the S-wave $\bar{K}N$ models

The differential cross sections at $|\vec{p}_K| = 1$ GeV are also predicted in Ref. [34]. We first note that our predicted cross sections shown in Fig. 6 are much larger than those given in Fig. 12 of Ref. [34]. We find that it is mainly due to the large difference between the amplitudes used in the calculations of $\bar{K}N_2 \to \bar{K}^{ex}N$ in the $\bar{K}$-exchange process [Fig. 3(b)], where the incoming $\bar{K}$ has a large momentum. As seen in Fig. 5, the S-wave $\bar{K}N$ model used in Ref. [34] underestimates the $\bar{K}N \to \bar{K}N$ cross section greatly in the invariant-mass region around $W = 1.8$ GeV, which is covered in the loop integration of Eq. (20) over the momentum of the nucleon in the deuteron. In such a high-W region far beyond the $\bar{K}N$ threshold, it is necessary to include the higher partial-wave contributions. This can be understood from Fig. 5 where we compare the $K^-p \to \bar{K}^0n$ cross sections from our DCC model and the two S-wave models of Refs. [34, 38]. If we keep only the S-wave part of the amplitude in our calculation, our results (solid curve) in Fig. 5 are actually reduced to the values close to the results (dot-dashed and dotted curves) of the two S-wave models. Accordingly, we see in Fig. 13 that the magnitude of $d\sigma/(dM_{\pi\Sigma}d\Omega_{p_n})$ for the $K^-d \to \pi\Sigma n$ reactions are drastically reduced if we include only the S-wave amplitudes for $\bar{K}N_2 \to \bar{K}^{ex}N$ in the $\bar{K}$-exchange process. This result indicates that the use of appropriate amplitudes that reproduce the $\bar{K}N$ reactions up to a very high energy is inevitable for obtaining the K^-d reaction cross sections that are comparable with the experimental data. The same argument would also apply to the other studies of the K^-d reaction [31–33], where the amplitudes for the meson-baryon subprocesses are obtained by fitting only to the near-threshold data of $\bar{K}N$ reactions. It is noted that the higher-order scattering processes were also taken into account in Ref. [34]. By performing calculations using their S-wave $\bar{K}N$ model, however, we confirm that in the considered kinematics their results are nearly saturated by the impulse and $\bar{K}$-exchange processes and the higher-order effects seem subdominant. Therefore, the use of appropriate $\bar{K}N$ scattering amplitudes, which can make the K^-d reaction cross sections
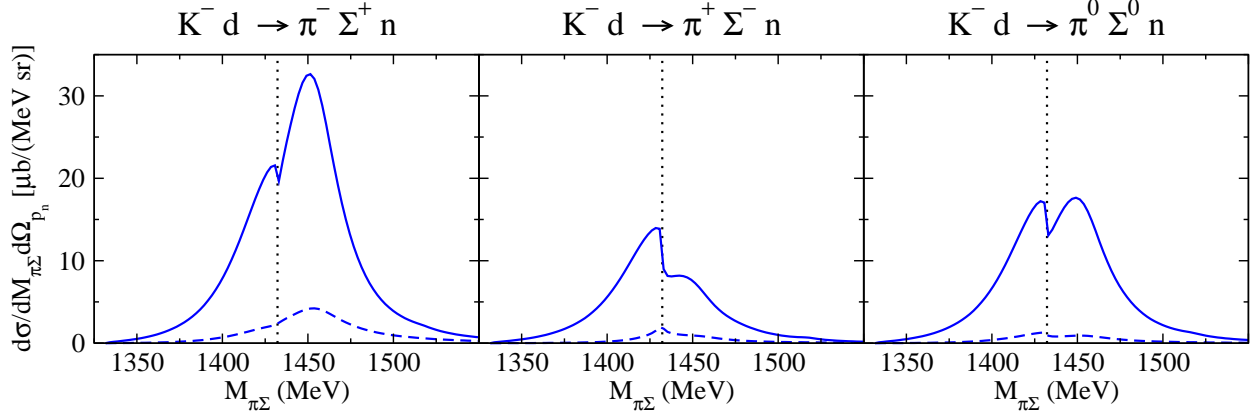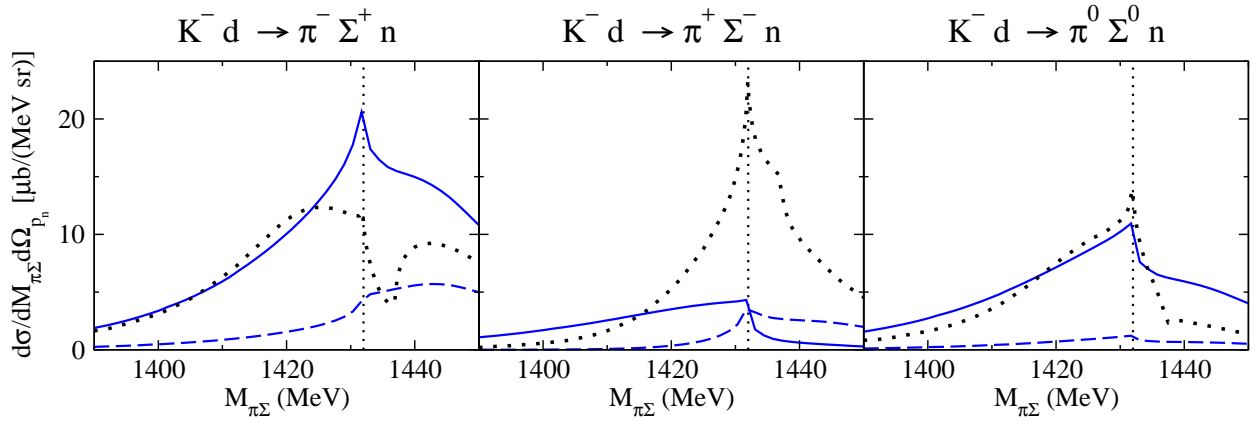
FIG. 13. Threefold differential cross section $d\sigma/(dM_{\pi\Sigma}d\Omega_{p_n})$ for the $K^-d \to \pi\Sigma n$ reactions at $|\vec{p}_{K^-}| = 1$ GeV and $\theta_{p_n} = 0$. Solid curves represent the full result, while dashed curves represent the results in which only the S-wave amplitudes are included for $\bar{K}N_2 \to \bar{K}^{\mathrm{ex}}N$ of the $\bar{K}$-exchange process. Dotted vertical lines indicate the $\pi\Sigma$ invariant mass at the $\bar{K}N$ threshold.

FIG. 14. Threefold differential cross section $d\sigma/(dM_{\pi\Sigma}d\Omega_{p_n})$ for the $K^-d \to \pi\Sigma n$ reactions at $|\vec{p}_{K^-}| = 0.6$ GeV and $\theta_{p_n} = 0$. Solid curves are the full results from our Model B, while dashed curves are the results from Model B in which only the the S-wave amplitudes are included for all meson-baryon subprocesses. Dotted curves are the results in Ref. [31], where the S-wave $\bar{K}N$ model developed in Ref. [38] are used for calculating the meson-baryon subprocesses. Dotted vertical lines indicate the $\pi\Sigma$ invariant mass at the $\bar{K}N$ threshold.

360   order(s) of magnitude larger, seems more important than the higher-order effects.

361   We next compare our results at $|\vec{p}_K| = 0.6$ GeV with those given in Ref. [31]. In Fig. 14,
362 we see that our "S-wave only" results at $|\vec{p}_{\bar{K}}| = 0.6$ GeV are much smaller than the results
363 in Ref. [31]. The results in Ref. [31] are even comparable or larger than our full results
364 in which higher partial waves are also included. This can be understood from Fig. 15.
365 For the $\bar{K}N_2 \to \bar{K}^{\mathrm{ex}}N$ subprocess, the $K^-p \to \bar{K}^0n$ and $K^-n \to K^-n$ charge states can
366 contribute. We see that at $W \sim 1.6$ GeV, which corresponds to a typical invariant mass of
367 the $\bar{K}N_2 \to \bar{K}^{\mathrm{ex}}N$ subprocess for $|\vec{p}_{\bar{K}}| = 0.6$ GeV, the S-wave $\bar{K}N$ model used in Ref. [31]
368 gives a large cross section for $K^-n \to K^-n$, which is even larger than our full results. Since
369 all the $\bar{K}N$ models give similar cross sections near the threshold, we can conclude that this
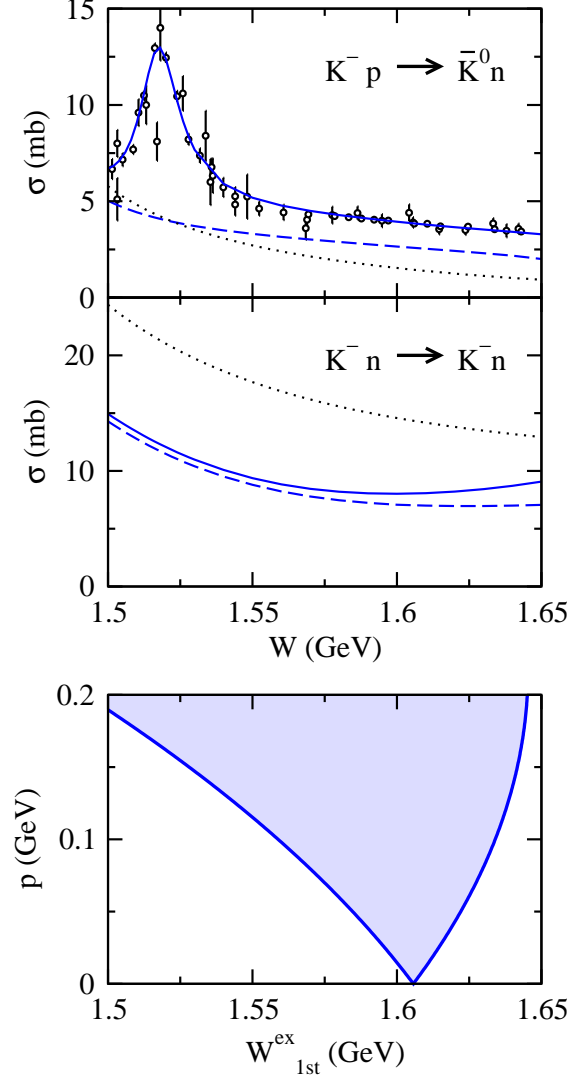
17

FIG. 15. Upper panel: Total cross section for $K^-p \to \bar{K}^0n$ in the energy region relevant to the $\bar{K}N_2 \to \bar{K}^{ex}N$ subprocess in the $\bar{K}$-exchange process [Fig. 3(b)] for the case of $|\vec{p}_{\bar{K}}| = 0.6$ GeV and $\theta_{p_N} = 0$. Solid (dashed) curve is the full (S-wave only) result from Model B of Ref. [2], while dotted curve is from the model developed in Ref. [38] that was used for the calculation in Refs. [31–33]. Middle panel: Same as the upper panel but for $K^-n \to \bar{K}^-n$. Lower panel: Allowed ranges of the invariant mass W_{1st}^{ex} for the $\bar{K}N_2 \to \bar{K}^{ex}N$ subprocess as $p \equiv |-\vec{p}|$ is varied. Here the incoming-$\bar{K}$ momentum and the scattering angle of outgoing N are fixed as $|\vec{p}_{\bar{K}}| = 0.6$ GeV and $\theta_{p_N} = 0$.

370 is the origin of the large $K^-d \to \pi\Sigma n$ reaction cross section found in Ref. [31]. Furthermore,
371 the $K^-n \to K^-n$ cross sections are larger than $K^-p \to K^0n$ cross sections and thus has
372 a larger contribution to the $\bar{K}$-exchange amplitudes. This is why the result from Ref. [31]
373 has a large cross section for $K^-d \to \pi\Sigma n$ at $p_K = 0.6$ GeV. This observation also indicates
374 that one must use the $\bar{K}N$ amplitudes that are well tested by the $\bar{K}N$ reaction data up to
375 a high energy region far beyond the $\bar{K}N$ threshold.

IV. SUMMARY AND FUTURE DEVELOPMENTS

Aiming at establishing low-lying Y^* resonances through analyzing the forthcoming data from the J-PARC E31 experiment, we have developed a model for the $\bar{K}d \to \pi Y N$ reaction. At the kinematics of this experiment that the outgoing nucleon is in the direction of the incoming $\bar{K}$, the cross sections for this reaction are dominated by the $\bar{K}$-exchange mechanism. The amplitudes of this $\bar{K}$-exchange process are calculated in our approach by using the off-shell amplitudes of $\bar{K}N \to \bar{K}N$ and $\bar{K}N \to \pi Y$ generated from the dynamical coupled-channels (DCC) model developed in Ref. [2]. This DCC model was constructed by fitting the existing data of $K^- p \to \bar{K}N, \pi\Sigma, \pi\Lambda, \eta\Lambda, K\Xi$ reactions over the wide energy region from the thresholds up to $W = 2.1$ GeV.

Most previous works used elementary meson-baryon amplitudes that were constructed by fitting only to the $\bar{K}N$ reaction data near the threshold. However, we have shown that if the incoming-$\bar{K}$ momentum is rather high as in the case of the J-PARC E31 experiment, the use of such amplitudes would result in the cross section that is order(s) of magnitude smaller than the one calculated using the appropriate meson-baryon amplitudes that reproduce the $\bar{K}N$ reactions in the energy region far beyond the $\bar{K}N$ threshold. This is because the meson-baryon subprocess produced by the reaction between the incoming $\bar{K}$ and the nucleon inside of the deuteron can have a very high invariant mass, even if the invariant mass of the final πY system is quite low.

We have shown that the $\bar{K}d \to \pi Y N$ reactions are useful for studying low-lying Y^* resonances. In fact, by comparing the results between our two models, Model A and Model B, we have found that the behavior of the threefold differential cross sections for $K^- d \to \pi \Sigma n$ [$K^- d \to \pi^- \Lambda p$] below the $\bar{K}N$ threshold are sensitive to the existence and position of the S_{01} resonance poles including $\Lambda(1405)1/2^-$ [the P_{13} resonance poles including $\Sigma(1385)3/2^+$]. We have also demonstrated that the $K^- d \to \pi^- \Lambda p$ reaction data would provide useful information for judging the existence of an unestablished low-lying $J^P = 1/2^+$ Σ resonance with the pole mass $M_R = 1457 - i39$ MeV, which is currently found only in Model B.

Here we note that we have followed the previous works [31–33] to consider only the impulse and $\bar{K}$-exchange processes and ignore other higher-order three-particle final state interactions. One possible important correction is the π-exchange mechanism when the invariant mass of the outgoing πN state in the final $\pi Y N$ state is near the $\Delta(1232)$ region. We have found that it has negligible effects to change our results in the considered special kinematics shown in Fig. 1. Nevertheless, our results on the differences between Models A and B should be further quantified by performing the complete three-particle calculation. This is, however, rather difficult within the framework using the $\bar{K}N$ amplitudes of the DCC model of Ref. [2] mainly because of the presence of multi-channel final states, such as $\pi\Lambda N$, $\pi\Sigma N$, $\eta\Lambda N$, and $K\Xi N$, and of the non-separable nature of our meson-baryon amplitudes, which is different from those used in Ref. [34] where the separable nature of the two-body amplitudes was a key to solving the three-body scattering equation. Clearly, this requires a separated long-term effort.

A necessary and immediate next step towards constructing a reliable $\bar{K}d$ reaction model that can be used for the spectroscopic study of low-lying Y^* resonances would be to include the baryon-exchange processes in addition to $\bar{K}$- and π-exchange processes, so that we can apply our $\bar{K}d$ reaction model to wider kinematical region. Also, the inclusion of baryon-exchange process would make our model applicable to the study of YN and YY interactions, where the latter is quite interesting in relation to a possible existence of the H dibaryons.

Our investigations in this direction will be presented elsewhere.

[1] H. Zhang, J. Tulpan, M. Shrestha, and D. M. Manley, Phys. Rev. C **88**, 035204 (2013); 035205 (2013).

[2] H. Kamano, S. X. Nakamura, T.-S. H. Lee, and T. Sato, Phys. Rev. C **90**, 065204 (2014).

[3] H. Kamano, S. X. Nakamura, T.-S. H. Lee, and T. Sato, Phys. Rev. C **92**, 025205 (2015).

[4] C. Fernandez-Ramirez, I. V. Danilkin, D. M. Manley, V. Mathieu, and A. P. Szczepaniak, Phys. Rev. D **93**, 034029 (2016).

[5] R. de la Madrid, Nucl. Phys. **A812**, 13 (2008); R. de la Madrid and M. Gadella, Am. J. Phys. **70**, 626 (2002); references therein.

[6] K. A. Olive *et al.* (Particle Data Group), Chin. Phys. C **38**, 090001 (2014).

[7] D. J. Wilson, J. J. Dudek, R. G. Edwards, and C. E. Thomas, Phys. Rev. D **91** 054008 (2015); D. J. Wilson, R. A. Briceno, J. J. Dudek, R. G. Edwards, and C. E. Thomas, Phys. Rev. D **92**, 094502 (2015); J. J. Dudek, R. G. Edwards, and D. J. Wilson, Phys. Rev. D **93**, 094506 (2016).

[8] J. M. M. Hall, A. C.-P. Hsu, D. B. Leinweber, A. W. Thomas, and R. D. Young, Phys. Rev. D **87**, 094510 (2013); J. J. Wu, T.-S. H. Lee, A. W. Thomas, and R. D. Young, Phys. Rev. C **90**, 055206 (2014); Z. W. Liu, W. Kamleh, D. B. Leinweber, F. M. Stokes, A. W. Thomas, and J. J. Wu, Phys. Rev. Lett. **116**, 082004 (2016).

[9] R. Molina and M. Döring, arXiv:1512.05831.

[10] A. Matsuyama, T. Sato, and T.-S. H. Lee, Phys. Rep. **439**, 193 (2007).

[11] B. Juliá-Díaz, T.-S. H. Lee, A. Matsuyama, and T. Sato, Phys. Rev. C **76**, 065201 (2007).

[12] B. Juliá-Díaz, T.-S. H. Lee,A. Matsuyama, T. Sato, and L. C. Smith, Phys. Rev. C **77**, 045205 (2008).

[13] J. Durand, B. Julia-Diaz, T.-S. H. Lee, B. Saghai, and T. Sato, Phys. Rev. C **78**, 025204 (2008).

[14] H. Kamano, B. Juliá-Díaz, T.-S. H. Lee, A. Matsuyama, and T. Sato, Phys. Rev. C **79**, 025206 (2009).

[15] B. Juliá-Díaz, H. Kamano, T.-S. H. Lee, A. Matsuyama, T. Sato, and N. Suzuki, Phys. Rev. C **80**, 025207 (2009).

[16] H. Kamano, B. Juliá-Díaz, T.-S. H. Lee, A. Matsuyama, and T. Sato, Phys. Rev. C **80**, 065203 (2009).

[17] N. Suzuki, B. Juliá-Díaz, H. Kamano, T.-S. H. Lee, A. Matsuyama, and T. Sato, Phys. Rev. Lett. **104**, 042302 (2010).

[18] N. Suzuki, T. Sato, and T.-S. H. Lee, Phys. Rev. C **82** 045206 (2010).

[19] H. Kamano, S. X. Nakamura, T.-S. H. Lee, and T. Sato, Phys. Rev. C **81**, 065207 (2010).

[20] H. Kamano, S. X. Nakamura, T.-S. H. Lee, and T. Sato, Phys. Rev. D **86**, 097503 (2012).

[21] H. Kamano, S. X. Nakamura, T.-S. H. Lee, and T. Sato, Phys. Rev. C **88**, 035209 (2013).

[22] H. Kamano, Phys. Rev. C **88**, 045203 (2013).

[23] S. X. Nakamura, H. Kamano, and T. Sato, Phys. Rev. D **92**, 074024 (2015).

[24] H. Kamano, S. X. Nakamura, T.-S. H. Lee, and T. Sato, Phys. Rev. C **94**, 015201 (2016).

[25] J. A. Oller and U.-G. Meißner, Phys. Lett. **B500**, 263 (2001).

[26] Y. Ikeda, T. Hyodo, D. Jido, H. Kamano, T. Sato, and K. Yazaki, Prog. Theor. Phys. **125**, 1205 (2011).

[27] J. Haidenbauer, G. Krein, U.-G. Meißner, and L. Tolos, Eur. Phys. J. A **47**, 18 (2011).

[28] M. L. Goldberger and K. M. Watson, *Collision Theory* (John Wiley & Sons, New York, 1964).

[29] H. Feshbach *Theoretical Nuclear Physics, Nuclear Reactions* (Wiley, New York, 1992).

[30] H. Noumi *et al.*, Spectroscopic study of hyperon resonances below $\bar{K}N$ threshold via the (K^-, n) reaction on deuteron (J-PARC E31), http://j-parc.jp/researcher/Hadron/en/pac_1207/pdf/E31_2012-9.pdf .

[31] K. Miyagawa and J. Haidenbauer, Phys. Rev. C **85**, 065201 (2012).

[32] D. Jido, E. Oset, and T. Sekihara, Eur. Phys. J. A **42**, 257 (2009); **49**, 95 (2013);

[33] J. Yamagata-Sekihara, T. Sekihara, and D. Jido, PTEP **2013**, 043D02 (2013).

[34] S. Ohnishi, Y. Ikeda, T. Hyodo, and W. Weise, Phys. Rev. C **93**, 025207 (2016).

[35] R. B. Wiringa, V. G. J. Stoks, and R. Schiavilla Phys. Rev. C **51**, 38 (1995)

[36] E. O. Alt, P. Grassberger, and W. Sandhas, Nucl. Phys. **B2**, 167 (1967).

[37] J. J. Wu, T. Sato and T.-S. H. Lee, Phys. Rev. C **91**, 035203 (2015).

[38] E. Oset and A. Ramos, Nucl. Phys. **A635**, 99 (1998).

[39] H. Noumi (private communication).